Melina Witt, Judith Bönnighausen, Fabian Eustermann, Aline Savourat, Jan P. Scheifers, Boniface P.T. Fokwa, Carsten Doerenkamp, Hellmut Eckert and Oliver Janka*

Extending the knowledge on the quaternary rare earth nickel aluminum germanides of the *RE*$NiAl_4Ge_2$ series (*RE* = Y, Sm, Gd–Tm, Lu) – structural, magnetic and NMR-spectroscopic investigations

https://doi.org/10.1515/znb-2019-0176
Received November 5, 2019; accepted November 14, 2019

Abstract: The quaternary rare earth nickel aluminum germanide series $RENiAl_4Ge_2$ (*RE* = Y, Sm, Gd–Tm, Lu) has been extended by several members. The compounds were synthesized from the elements by arc-melting, and single crystals of $YNiAl_4Ge_2$, $GdNiAl_4Ge_2$, and $LuNiAl_4Ge_2$ were grown from an aluminum flux. All members crystallize isostructurally in the rhombohedral $SmNiAl_4Ge_2$-type structure ($R\bar{3}m$, $Z = 3$). The compounds can be described as a stacking of $RE^{\delta+}$ and $[NiAl_4Ge_2]^{\delta-}$ slabs with an ABC stacking sequence, or alternatively as stacking of CsCl and CdI_2 building blocks. The results of the magnetic measurements indicate that all rare earth atoms are in a trivalent oxidation state. Of the $RENiAl_4Ge_2$ series, the members with *RE* = Sm, Gd–Dy exhibit antiferromagnetic ordering with a maximum Néel temperature of $T_N = 16.4(1)$ K observed for $GdNiAl_4Ge_2$. ^{27}Al NMR spectroscopic investigations yielded spectra with two distinct signals, in line with the crystal structure, however, significantly different resonance frequencies of $\delta_{iso}^{ms}(YNiAl_4Ge_2) = 77(1)$ and 482(1) ppm as well as $\delta_{iso}^{ms}(LuNiAl_4Ge_2) = 90(1)$ and 467(1) ppm were observed. These indicate significantly different *s*-electron densities at the two crystallographically different Al atoms, in line with the results from DFT calculations. The Bader charge analysis confirms that the present compounds must be considered as germanides, as expected from the relative electronegativities of the constituent elements, while the low charges on Al and Y indicate significant covalent bonding.

Keywords: aluminum; DFT calculations; germanium; intermetallics; magnetic properties; nickel; rare earth elements; solid-state NMR spectroscopy.

Dedicated to: Professor Arndt Simon on the occasion of his 80th birthday.

1 Introduction

Binary and ternary intermetallic compounds of the rare earth elements have been studied extensively [1–3]. The most prominent structure type for the binaries is the cubic Laves phase $MgCu_2$ [4], followed by the Cu_3Au [5], the $CaCu_5$ [6], the NaCl [7] and the CsCl type [8]. For these structure types, several thousands of compounds are reported in the Pearson database [9]. The structural variety increases further when adding a third element. For the ternary structure types, $ThCr_2Si_2$ [10], $CaBe_2Ge_2$ [11], TiNiSi [12] and ZrNiAl [13] are the most prominent ones. Amongst these, especially the cerium compounds have gained a lot of attention due to their intriguing physical properties. For the equiatomic compounds, these have been summarized in a series of review articles [14–17]. Quaternary intermetallic compounds, however, have not been studied in this great detail yet. Due to our interest in the crystal structures and the physical and NMR spectroscopic properties [18] of intermetallic aluminum compounds of the alkali (Na_2Au_3Al [19]), alkaline earth (e.g. MAu_2Al_2 with *M* = Ca, Sr [20]; *M*Au*X* with *M* = Ca–Ba and *X* = Al–In [21]; $MPtAl_2$ with *M* = Ca–Ba [22]) and the rare earth elements (e.g. RET_5Al_2 with *RE* = Y, Gd–Tm, Lu and *T* = Pd, Pt [23], RE_2TAl_3 with *RE* = Y, La–Nd, Sm, Gd–Lu and *T* = Ru, Rh, Ir [24], $Eu_2Pt_6Al_{15}$ [25], $Eu_2Ir_3Al_9$ [26] or $YbPd_2Al_3$ [27]), the interest of extending the knowledge of quaternary aluminum containing compounds has sparked. Amongst

---

***Corresponding author: Oliver Janka,** Institut für Anorganische und Analytische Chemie, Westfälische Wilhelms-Universität Münster, Corrensstrasse 28/30, 48149 Münster, Germany, Tel.: +49(0)251-83-36074, Fax: +49(0)251-83-36002, E-mail: ocjanka@uni-muenster.de
Melina Witt, Judith Bönnighausen, Fabian Eustermann and Aline Savourat: Institut für Anorganische und Analytische Chemie, Westfälische Wilhelms-Universität Münster, Corrensstrasse 28/30, 48149 Münster, Germany
Jan P. Scheifers and Boniface P.T. Fokwa: University of California Riverside, Department of Chemistry, 501 Box Springs Rd, Riverside, CA 92521, USA
Carsten Doerenkamp: Instituto de Física de São Carlos, Universidade de São Paulo, São Carlos, SP 13566-590, Brazil
Hellmut Eckert: Instituto de Física de São Carlos, Universidade de São Paulo, São Carlos, SP 13566-590, Brazil; and Institut für Physikalische Chemie, Westfälische Wilhelms-Universität Münster, Corrensstrasse 28, 48149 Münster, Germany

the vast number of potential elemental combinations, the aluminum germanides of the rare earth elements were chosen due to the pronounced differences in the electron count of the respective elements, enabling single-crystal X-ray diffraction experiments. For the quaternary system RE–T–Al–Ge with RE = Sc, Y, La–Nd, Sm–Lu and T being a late transition metal of the Fe, Co, Ni or Cu group, only a limited number of compounds with full ordering of the constituent elements have been reported. These are the $\mathrm{Ce}_2T\mathrm{Al}_7\mathrm{Ge}_4$ series (T = Co, Ni, Pd, Ir; $\mathrm{Ce_2CoAl_7Ge_4}$ type) [28], $\mathrm{Er_5Ni_3Al_3Ge_4}$ (own type, sole example) [29], the $RE_2T\mathrm{Al}_4\mathrm{Ge}_2$ (RE = Y, Sm, Gd–Lu, T = Fe–Ni, $\mathrm{Tb_2NiAl_4Ge_2}$ type) [30–33] and $RE_3T\mathrm{Al}_3\mathrm{Ge}_2$ series (RE = Y, Sm, Gd–Lu, T = Mn–Cu, $\mathrm{Y_3NiAl_3Ge_2}$ type) [34–39], and finally the $RET\mathrm{Al}_4\mathrm{Ge}_2$ compounds (RE = Y, Ce, Nd, Sm, Gd, Er, T = Ni, Au) with the $\mathrm{SmNiAl_4Ge_2}$-type structure [31, 40, 41]. One interesting structural feature is that all named compounds, with the exception of $\mathrm{Er_5Ni_3Al_3Ge_4}$, exhibit no bonding RE–T interactions, in contrast to many of the ternary intermetallics. As another structurally interesting characteristic of these compounds, all of them exhibit rather short Al–Ge distances between 260 and 280 pm, suggesting at least weak bonding interactions (sum of the covalent radii $\Sigma(r_{\mathrm{cov}})$ = Al + Ge = 125 + 122 = 247 pm). However, no ordered binary aluminum germanides are known. Here we report on the synthesis and the structural, magnetic, ^{27}Al NMR spectroscopic and theoretical (DFT level) characterization of several new members of the $RE\mathrm{NiAl_4Ge_2}$ series (RE = Y, Sm, Gd–Tm, Lu).

2 Experimental

2.1 Synthesis

The $RE\mathrm{NiAl_4Ge_2}$ (RE = Y, Sm, Gd–Tm, Lu) members were synthesized from the elements using arc-melting techniques. Starting materials were rare earth ingots (Sigma-Aldrich, Smart Elements, 99.9%), nickel wire (Alfa Aesar, 99.9%), aluminum turnings (Koch Chemicals, 99.99%) and germanium chunks (Chempur, 99.999%). The starting materials were weighed in the ideal stoichiometry of 1:1:4:2 (RE:Ni:Al:Ge) and arc-melted under an argon atmosphere of about 800 mbar [42]. The obtained buttons were re-melted several times to increase the homogeneity. The samples were subsequently enclosed in evacuated quartz tubes and annealed in a second step (973 K, 14 d) to increase their overall phase purity and homogeneity. The annealing led to X-ray pure samples, suitable for physical property measurements. All samples obtained by these processes show metallic luster and are stable under ambient conditions over weeks. In order to obtain single crystals, the method published by Sieve et al. [41] was employed. The elements were weighed in a ratio of 1:1:10:5 (RE:Ni:Al:Ge) into aluminum oxide crucibles. These were sealed in evacuated quartz tubes and heated to T = 1073 K for 4 days. Afterwards, the samples were cooled to T = 773 K with 2 K h^{-1}. The excess aluminum flux was dissolved in 5 M NaOH, leaving behind well shaped single crystals along with unreacted germanium. These flux-grown crystals were used for the structure determination experiments.

2.2 X-ray diffraction

The annealed polycrystalline samples were analyzed by powder X-ray diffraction experiments: Guinier technique, imaging plate system (Fuji film, BAS 1800), Cu$K\alpha_1$ radiation and α-quartz (a = 491.30 and c = 540.46 pm) as internal standard. The trigonal lattice parameters were obtained by least-squares refinements on the basis of the $\mathrm{YNiAl_4Ge_2}$ data set from the literature (Table 1). Crystals of $\mathrm{YNiAl_4Ge_2}$, $\mathrm{GdNiAl_4Ge_2}$ and $\mathrm{LuNiAl_4Ge_2}$, grown from Al flux, were glued to thin quartz fibers using beeswax. The crystallite quality was checked by Laue photographs on a Buerger precession camera (white molybdenum radiation; imaging plate system, Fuji film, BAS 1800). Intensity data sets of suitable single crystals were collected at room temperature on an IPDS-II (graphite-monochromatized Mo$K\alpha$ radiation; λ = 71.073 pm; oscillation mode). Numerical absorption corrections were applied to all data sets. Details of the data collection and structure refinements can be found in Tables 2–4.

Table 1: Lattice parameters of the rhombohedral $RE\mathrm{NiAl_4Ge_2}$ series (RE = Y, Sm, Gd–Tm, Lu), space group $R\bar{3}m$, Z = 3, $\mathrm{SmNiAl_4Ge_2}$ type.

Compound	*a* (pm)	*c* (pm)	*V* (nm^3)
$\mathrm{YNiAl_4Ge_2}^{a}$	408.3(1)	3084.5(3)	0.4453
$\mathrm{YNiAl_4Ge_2}$ [41]	409.59(11)	3095.8(11)	0.4497
$\mathrm{SmNiAl_4Ge_2}^{a}$	410.6(1)	3105.5(2)	0.4535
$\mathrm{SmNiAl_4Ge_2}$ [41]	411.21(6)	3111.09(6)	0.4556
$\mathrm{GdNiAl_4Ge_2}^{a}$	409.5(1)	3097.3(2)	0.4497
$\mathrm{TbNiAl_4Ge_2}^{a}$	408.5(1)	3085.7(2)	0.4459
$\mathrm{DyNiAl_4Ge_2}^{a}$	408.0(1)	3080.7(3)	0.4440
$\mathrm{HoNiAl_4Ge_2}^{a}$	407.5(1)	3074.4(3)	0.4422
$\mathrm{ErNiAl_4Ge_2}^{a}$	407.2(1)	3072.2(2)	0.4411
$\mathrm{ErNiAl_4Ge_2}$ [31]	407.16(8)	3070.27(9)	0.4408
$\mathrm{TmNiAl_4Ge_2}^{a}$	406.8(1)	3068.1(2)	0.4398
$\mathrm{LuNiAl_4Ge_2}^{a}$	406.1(1)	3059.5(1)	0.4369

^{a}This work.

Table 2: Crystallographic data and structure refinement for $YNiAl_4Ge_2$, $GdNiAl_4Ge_2$, and $LuNiAl_4Ge_2$, space group $R\bar{3}m$, $Z=3$, $SmNiAl_4Ge_2$ type.

Formula	$YNiAl_4Ge_2$	$GdNiAl_4Ge_2$	$LuNiAl_4Ge_2$
Molar mass, g mol^{-1}	400.7	469.0	486.8
Lattice parameters	See Table 1	See Table 1	See Table 1
Density calc., g cm^{-3}	4.48	5.19	5.55
Crystal size, µm	120 × 60 × 60	90 × 80 × 70	130 × 60 × 45
Diffractometer	Stoe IPDS-II	Stoe IPDS-II	Stoe IPDS-II
Wavelength/λ, pm	Mo$K\alpha$/71.073	Mo$K\alpha$/71.073	Mo$K\alpha$/71.073
Transmission ratio (min/max)	0.382/0.733	0.401/0.539	0.197/0.591
Detector distance, mm	70	80	80
Exposure time, min	7	5	3
Integr. param. A/B/EMS	14.0/−1.0/0.030	14.0/−1.0/0.030	14.0/−1.0/0.030
$F(000)$, e	549	624	645
Range in hkl	±6; −5, +6; −46, +43	±6; −5, +6; −40, +45	±6; −5, +6; −40, +45
$\theta_{min}/\theta_{max}$, °	4.0/33.2	2.0/31.7	2.0/31.8
Linear absorption coeff., mm^{-1}	23.3	24.3	30.6
Total no. of reflections	1767	1599	2673
Independent reflections/R_{int}	266/0.0241	237/0.0222	236/0.0266
Reflections with $I > \sigma(I)/R_\sigma$	244/0.0052	229/0.0047	225/0.0062
Data/parameters	266/15	237/15	236/15
$R1/wR2$ for $I > 3\sigma(I)$	0.0132/0.0313	0.0088/0.0226	0.0113/0.0257
$R1/wR2$ for all data	0.0159/0.0327	0.0093/0.0228	0.0125/0.0260
Goodness-of-fit on F^2	1.29	0.99	1.08
Extinction scheme	Lorentzian isotropic [43]	Lorentzian isotropic [43]	Lorentzian isotropic [43]
Extinction coefficient	950(50)	320(20)	800(30)
Diff. Fourier residues, e Å^{-3}	−0.50/+0.55	−0.35/+0.36	−1.22/+0.68

Table 3: Atom positions and equivalent isotropic displacement parameters (pm^2) for $YNiAl_4Ge_2$, $GdNiAl_4Ge_2$, and $LuNiAl_4Ge_2$, space group $R\bar{3}m$, $Z=3$, $SmNiAl_4Ge_2$ type.

Atom	Wyckoff position	z	U_{eq}	U_{11}	U_{33}	U_{12}
$YNiAl_4Ge_2$						
Y	3b	1/2	79(1)	78(3)	80(2)	39(1)
Ni	3a	0	56(1)	55(2)	58(2)	27(1)
Al1	6c	0.31088(3)	80(2)	76(2)	87(4)	38(1)
Al2	6c	0.07783(3)	84(2)	90(2)	72(4)	45(1)
Ge	6c	0.22303(1)	70(1)	70(1)	72(2)	35(1)
$GdNiAl_4Ge_2$						
Gd	3b	1/2	75(1)	74(1)	77(1)	37(1)
Ni	3a	0	56(1)	56(1)	56(2)	28(1)
Al1	6c	0.31099(3)	90(2)	80(2)	90(4)	45(1)
Al2	6c	0.07787(4)	93(2)	91(2)	98(4)	46(1)
Ge	6c	0.22369(1)	72(1)	71(1)	73(2)	36(1)
$LuNiAl_4Ge_2$						
Lu	3b	1/2	93(1)	93(1)	92(1)	47(1)
Ni	3a	0	71(1)	71(2)	71(3)	35(1)
Al1	6c	0.31050(4)	90(3)	84(3)	102(5)	42(2)
Al2	6c	0.07837(5)	99(3)	97(3)	102(5)	49(2)
Ge	6c	0.22158(1)	85(1)	84(1)	87(2)	42(1)

$x = y = 0$. U_{eq} is defined as one third of the trace of the orthogonalized U_{ij} tensor. Coefficients U_{ij} of the anisotropic displacement factor tensor of the atoms are defined by $-2\pi^2[(ha^*)^2U_{11} + \ldots + 2hka^*b^*U_{12}]$. $U_{11} = U_{22}$, $U_{13} = U_{23} = 0$.

CSD 1953918–1953920 contain the supplementary crystallographic data for this paper. The data can be obtained free of charge from The Cambridge Crystallographic Data Centre via www.ccdc.cam.ac.uk/structures.

2.3 Physical property measurements

Annealed pieces of the X-ray pure RENiAl$_4$Ge$_2$ (RE = Y, Sm, Gd–Tm, Lu) samples were attached to the sample holder rod of a vibrating sample magnetometer (VSM) using Kapton foil for measuring the magnetization $M(H,T)$ in a Quantum Design Physical Property Measurement System (PPMS). All samples were investigated in the temperature range of 2.5–300 K with applied external magnetic fields of up to 80 kOe (1 kOe = 7.96 × 10^4 A m^{-1}).

2.4 Solid-state NMR spectroscopy

^{27}Al solid-state NMR spectra of $YNiAl_4Ge_2$ and $LuNiAl_4Ge_2$ were recorded with a Bruker Avance Neo ($B_0 = 14.1$ T) and an Agilent DD2 ($B_0 = 5.7$ T) NMR spectrometer using magic-angle spinning rates between 37 and 40 kHz.

Table 4: Interatomic distances (pm) for $YNiAl_4Ge_2$, $GdNiAl_4Ge_2$, and $LuNiAl_4Ge_2$, space group $R\bar{3}m$, $Z = 3$, $SmNiAl_4Ge_2$ type.

$YNiAl_4Ge_2$							
Y	Ge	6	293.0	Ni	Al2	2	240.0
	Al2	6	361.5		Al1	6	245.7
Al1	Ni	3	245.7	Al2	Ni	1	240.0
	Ge	1	270.9		Ge	3	256.1
	Al1	3	273.5		Al1	3	291.1
	Al2	3	291.1		Y	3	361.5
Ge	Al2	3	256.1				
	Al1	1	270.9				
	Y	3	293.0				
$GdNiAl_4Ge_2$							
Gd	Ge	6	295.2	Ni	Al2	2	241.0
	Al2	6	362.7		Al1	6	246.6
Al1	Ni	3	246.6	Al2	Ni	1	241.0
	Ge	1	270.1		Ge	3	256.2
	Al1	3	274.2		Al1	3	292.5
	Al2	3	292.5		Gd	3	362.7
Ge	Al2	3	256.2				
	Al1	1	270.1				
	Gd	3	295.2				
$LuNiAl_4Ge_2$							
Lu	Ge	6	288.5	Ni	Al2	2	240.0
	Al2	6	357.8		Al1	6	244.6
Al1	Ni	3	244.6	Al2	Ni	1	240.0
	Ge	1	272.4		Ge	3	255.8
	Al1	3	272.9		Al1	3	289.7
	Al2	3	289.7		Lu	3	357.8
Ge	Al2	3	255.8				
	Al1	1	272.4				
	Lu	3	288.5				

All distances of the first coordination sphere are listed. All standard uncertainties were less than 0.1 pm.

To reduce the electrical conductivity and density, the finely powdered samples were mixed in approximate volume ratios of 1:2 with dry potassium bromide and filled into a conventional ZrO_2 MAS rotor with 1.3 or 1.6 mm diameter. The spectra were recorded using conventional single-pulse experiments with typical pulse lengths of 0.1–0.5 µs (corresponding to flip angles below 30°) and relaxation delays of 0.1 s. Triple-quantum (TQ-) MAS-NMR spectra were recorded at 14.1 T, at a spinning speed of 35.0 kHz using the standard three-pulse zero-filtering sequence. The high-power (90 W) excitation and reconversion pulses were 1.8 and 0.6 µs long, and were followed by a weak (0.6 W) detection pulse of 7 µs length. A relaxation delay of 100 ms was used. Solid AlF_3 was used as secondary standard (–16 ppm) [44], referring to a 1 molar aqueous solution of $Al(NO_3)_3$. Data was processed and simulated with the DMFIT program [45].

2.5 Quantum-chemical calculations

Electronic structure calculations, using the experimentally obtained structure of $YNiAl_4Ge_2$ from the literature [41] and the single-crystal data of $LuNiAl_4Ge_2$ presented here, were performed using the projector augmented wave method (PAW) of Blöchl [46, 47] coded in the Vienna *ab initio* simulation package (VASP) [48, 49]. All VASP calculations employed the generalized gradient approximation (GGA) using the exchange-correlation functional by Perdew-Burke-Ernzerhof (PBE) [50]. The cut-off energy for the plane wave calculations was set to 500 eV and the Brillouin zone integration was carried out using a $15 \times 15 \times 3$ Γ-centered k-point mesh generated with the Monkhorst pack algorithm [51]. The subsequent Bader charge calculations, as developed by the Henkelman group, were based on the VASP results [52–54].

3 Results and discussion

3.1 Structure refinements

The obtained single crystal data sets showed rhombohedral lattices, and space group $R\bar{3}m$ was found to be correct during the structure refinements. Isotypism to the $SmNiAl_4Ge_2$-type structure was evident from both single crystal and powder X-ray diffraction experiments. Starting values for the structure refinements were obtained using the SUPERFLIP [55] program package, implemented in JANA2006 [56, 57]. All atomic positions and anisotropic displacement parameters were subsequently refined, again using the JANA2006 program package. Occupancy parameters of all crystallographic sites were individually refined in separate series of least-squares refinements in order to check for the correct composition. The final difference Fourier syntheses were featureless. The refined atomic parameters, displacement parameters and interatomic distances can be found in Tables 3 and 4.

3.2 Crystal chemistry

The quaternary rare earth nickel aluminum germanides of the $RE$$NiAl_4Ge_2$ series (RE = Y, Sm, Gd–Tm, Lu) crystallize in the rhombohedral $SmNiAl_4Ge_2$-type structure with space group $R\bar{3}m$ and $Z = 3$. As expected and shown in Fig. 1, the lattice parameters and unit cell volumes decrease nearly linearly when going from the gadolinium to the lutetium compound due to the lanthanide contraction. The

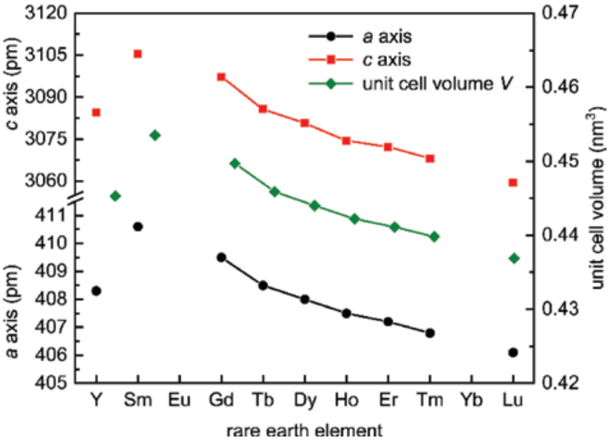

Fig. 1: Trigonal lattice parameters and unit cell volumes of the *RE*$NiAl_4Ge_2$ (*RE* = Y, Sm, Gd–Tm, Lu) series ($SmNiAl_4Ge_2$ type).

isostructural yttrium compound $YNiAl_4Ge_2$ exhibits lattice parameters similar to the ones of $TbNiAl_4Ge_2$, in line with the comparable ionic radii of the trivalent cations (Y^{3+}: 104 pm; Tb^{3+}: 102 pm; CN = 8 [58, 59]).

The following discussion of the crystal structure and the interatomic distances will be based on the refined single crystal data obtained for $GdNiAl_4Ge_2$. This crystal structure can be described in two ways. First by slabs of $[GdGe_2]^{\delta-}$ (CdI_2 type) and $[NiAl_4]^{\delta+}$ (CsCl type) as is shown in Fig. 2, left. This description is in line with the Bader charges (*vide supra*). Alternatively, one can utilize a bonding centered approach. By the interpretation of the interatomic distances, the Ni, Al and Ge atoms form polyanionic slabs with composition $[NiAl_4Ge_2]^{\delta-}$. These slabs are separated by the rare earth atoms and get stacked along [001] with an ABC sequence (Fig. 2, middle). The rare earth atoms exhibit coordination number CN = 12 and are surrounded by six Al and six Ge atoms (Fig. 3, top) in the shape of a distorted hexagonal prism with corrugated six-membered rings. The structure can be also described as an alternating intergrowth of CsCl- and Ce_2SO_2-type fragments, as depicted in Fig. 2 (middle). The interatomic distances are Gd–Al = 363 and Gd–Ge = 295 pm, suggesting no significant Gd–Al interactions and only weak Gd–Ge bonding (*vide infra*). No Gd–Ni contacts below 400 pm are observed. The Gd atoms form planar hexagonal densely packed layers (Fig. 2, right) with Gd–Gd distances of 410 pm, suggesting potential magnetic frustration (*vide infra*). Within the $[NiAl_4Ge_2]$ layers, the Ni atoms exhibit an eight-fold coordination solely by Al atoms. Six Al1 atoms form a cyclohexane like ring (Ni–Al1 = 247 pm), while the Al2 atoms cap its bottom and top (Ni–Al2 = 241 pm; Fig. 3, middle left). These distances are in the range of typical bonding interactions ($\Sigma(r_{cov})$ = Ni + Al = 115 + 125 = 240 pm) and comparable with those of NiAl (250 pm, CsCl type) or Ni_2Al_3 (244–254 pm,

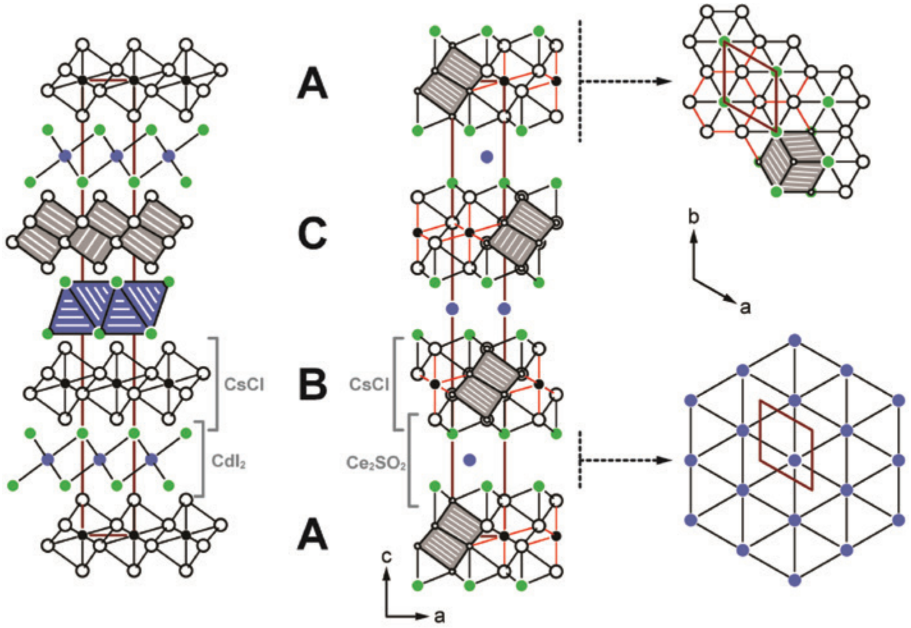

Fig. 2: Extended unit cell of $GdNiAl_4Ge_2$, depicted along the *b* axis. (left) Description as slabs of CsCl- and CdI_2-type. An ABC stacking sequence of both slabs is observed, the one for the CsCl layers is given. The distorted $Gd@Ge_6$ octahedra are shown in blue, the $Ni@Al_8$ cubes are drawn in grey. Gadolinium, nickel, aluminum, and germanium atoms are depicted as blue, black, open white and green circles, respectively. (middle) The layer-like arrangement of the $[NiAl_4Ge_2]^{\delta-}$ slabs is highlighted. Bonding in between the slabs has been omitted for clarity. (right) Views along the *c* axis on the $[NiAl_4Ge_2]^{\delta-}$ slabs (top) and the hexagonally closest packed gadolinium layers (bottom).

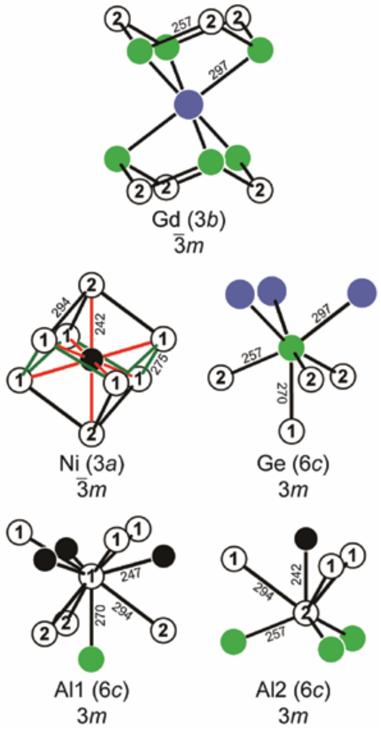

Fig. 3: Coordination environments surrounding the Gd (top), Ni (middle left), Ge (middle right), and Al atoms (bottom) in the crystal structure of $GdNiAl_4Ge_2$. Gadolinium, nickel, aluminum and germanium atoms are depicted as blue, black, open white, and green circles, respectively. Interatomic distances (in pm), Wyckoff sites and site symmetries are given.

own type). Alternatively, this coordination environment can be described as a distorted cube. The Al1–Al1 distances are 274 pm, while the Al1–Al2 distances are 292 pm. These entities form layers that get capped by the Ge atoms. The Ge atoms themselves are coordinated on one side by four Al atoms (3 × 256 + 1 × 270 pm) in a highly asymmetric mode (Fig. 3, middle right), while the other side of the Ge atoms is exposed to the Gd atoms (Gd–Ge = 295 pm) forming the outer layer of the $[NiAl_4Ge_2]$ slabs. Both, the Ge–Al and the Gd–Ge distances are slightly longer compared to the sum of the covalent radii ($\Sigma(r_{cov})$ = Ge + Al = 122 + 125 = 247 pm; $\Sigma(r_{cov})$ = Gd + Ge = 161 + 122 = 283 pm) and suggest weak interactions. Similar distances can be found in $Gd_2Al_3Ge_4$ (Gd–Ge = 302–318 pm, $Ba_2Cd_3Bi_4$ type) or Gd_5Ge_3 (299–307 pm, Mn_5Si_3 type). The coordination environments of Al1 and Al2 are depicted in Fig. 3, bottom.

3.3 Magnetic properties

The magnetic properties of the *RE*$NiAl_4Ge_2$ series (*RE* = Y, Sm, Gd–Tm, Lu) have been determined by susceptibility and magnetization experiments, the extracted data is listed in Table 5. Low-field measurements (20 Oe) of $YNiAl_4Ge_2$ and $LuNiAl_4Ge_2$ were conducted between T = 2.1–6 K. No superconductivity was observed, however. Both compounds exhibit nearly temperature-independent behavior (Fig. 4), indicating that all constituent elements exhibit closed shells. The upturn of the susceptibility at low temperatures originates from paramagnetic impurities (Curie tail). The susceptibilities at T = 300 K are $\chi_{300\,K}(YNiAl_4Ge_2) = -9.29(5) \times 10^{-5}$ emu mol^{-1} and $\chi_{300\,K}(LuNiAl_4Ge_2) = -1.23(5) \times 10^{-4}$ emu mol^{-1}. These negative values indicate that the intrinsic diamagnetism overcompensates the Pauli paramagnetism caused by the conduction electrons of the metallic materials.

The other compounds exhibit paramagnetism, solely arising from the open-shell $4f^n$ electron configuration of the rare earth atoms. As stated by Sieve and coworkers [41], the interatomic distances of the rare earth atoms suggest that the interactions within the layers (e.g. Er–Er = 407 pm [31]) are significantly stronger compared to the interlayer interactions (1077 pm [31]). However, due to the triangular arrangements of the rare earth atoms, geometrical spin frustration can arise [60, 61], leading to interesting magnetic phenomena, e.g. spin-glass behavior. All compounds were investigated by zero-field-cooled (ZFC) experiments with an applied external magnetic field of 10 kOe. The inverse susceptibility χ^{-1} was fitted using the modified Curie-Weiss law, and the effective magnetic moment μ_{eff} and the paramagnetic Curie temperature θ_P were extracted. In the case of $SmNiAl_4Ge_2$, the van Vleck theory was used. All compounds exhibit values for μ_{eff} that are close to those calculated (μ_{calcd}) for the free trivalent ions (see Table 5). The ordering temperatures (where observed) were further determined by low field (100 Oe) zero-field-cooled/field-cooled (ZFC/FC) measurements. The Néel temperatures of the paramagnetic→antiferromagnetic transitions were obtained from the observed peaks in the respective zero-field-cooled curves. Finally, magnetization isotherms above and below the magnetic ordering temperatures (where applicable) were recorded. The saturation magnetizations μ_{sat} were obtained from the 3 K isotherms at 80 kOe. Due to the polycrystalline character of all investigated samples, these values are for some compounds significantly lower compared to the theoretical values calculated according to $g_J \times J$. The small Weiss constants θ_P indicate weak (three-dimensional) magnetic interactions, in line with the large distances between the slabs. The positive signs could arise from a weak ferromagnetic coupling between these layers, suggesting so called A-type antiferromagnetism [62].

In the following paragraphs, the magnetic properties of the investigated compounds are discussed. For

Table 5: Magnetic properties of the rhombohedral *RE*NiAl$_4$Ge$_2$ (*RE* = Y, Sm, Gd–Tm, Lu) representatives, with T_N, Néel temperature; μ_{eff}, effective magnetic moment; θ_p, paramagnetic Curie temperature; μ_{sat}, saturation magnetization; H_{crit}, critical field of the meta-magnetic step.

RE	T_N (K)	μ_{eff} (μ_B)	μ_{calcd} (μ_B)	θ_p (K)	μ_{sat} (μ_B)	$g_J \times J$ (μ_B)	H_{crit} (kOe)
Y	χ(300 K) = −9.29(5) × 10^{-5} emu mol^{-1}						
Sm	15.9(1)	0.77(1)	0.845	−30.5(1)	0.05(1)	0.71	–
Gd	16.4(1)	8.09(1)	7.94	+1.2(1)	6.73(1)	7	–
Tb	9.7(1)	9.76(1)	9.72	+2.7(1)	6.61(1)	9	10(1)
Dy	10.6(1)	10.73(1)	10.65	−0.6(1)	7.79(1)	10	8.6(5)
Ho	6.2(1)	10.70(1)	10.61	+0.7(1)	8.21(1)	10	3.1(5)
Er	–	9.46(1)	9.58	−10.0(1)	4.00(1)	9	–
Tm	–	7.83(1)	7.56	−0.6(1)	4.00(1)	7	–
Lu	χ(300 K) = −1.23(5) × 10^{-4} emu mol^{-1}						

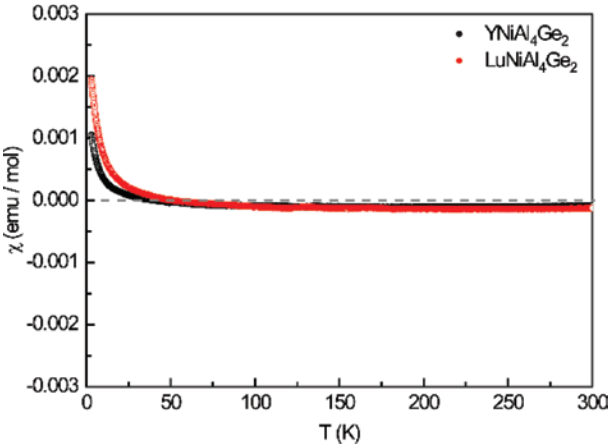

Fig. 4: Temperature dependence of the magnetic susceptibility of YNiAl$_4$Ge$_2$ (black) and LuNiAl$_4$Ge$_2$ (red).

SmNiAl$_4$Ge$_2$ these observations are, however, in contrast to the observations in the literature [41]. Sieve and coworkers observed a bifurcation between the ZFC and FC curves already near $T = 300$ K along with a pronounced hysteresis loop in the magnetization isotherms. We have observed that SmNiAl$_4$Ge$_2$ exhibits the expected van Vleck paramagnetism, along with antiferromagnetic ordering at low temperatures. The ZFC/FC measurements show only a minor splitting, possibly caused by trace impurities. The van Vleck behavior is caused by the close proximity of two states (ground state $J = 5/2$; excited state $J = 7/2$). The calculated energy difference between these states is only about 1550 K, all others of the respective angular momentum levels are considerably higher in energy. The small effective magnetic moment of the Sm^{3+} cations ($\mu_{eff,calcd} = 0.845$ μ_B) arises from the antiparallel coupling of the $L = 5$, $S = 5/2$ Russel-Saunders states. Stewart developed a theory to describe the magnetism of intermetallic samarium compounds, taking polarization effects, interionic Heisenberg exchange couplings and the population of the $J = 7/2$ and $J = 5/2$ ground states into account. Unexpectedly, a simple formula $\chi(T) = \chi_0 + D/(T - \theta)$ was derived [63]. Hamaker and coworkers were able to prove that $\chi(T)$ for polycrystalline SmRh$_4$B$_4$ can be described by the equation

$$\chi(T) = \frac{N_A}{k_B}\left(\frac{\mu_{eff}^2}{3(T - \theta_p)} + \frac{\mu_B^2}{\delta}\right)$$

where μ_{eff} is the effective magnetic moment, θ_p is the Weiss constant, μ_B is the Bohr magneton, N_A is the Avogadro number and k_B is the Boltzmann constant. δ is defined as $\delta = 7\Delta E/20$ in units of K and describes the energy differences of the ground and excited states. The first term represents the Curie-Weiss susceptibility of the $J = 5/2$ ground state, while the second part is the van Vleck susceptibility caused by the $J = 7/2$ multiplet, which is only slightly higher in energy [64]. Using the coefficients for the free ion values mentioned in the literature, this equation can be obtained from a more general one, that was published by Stewart [65]. It should be mentioned that both equations neglect crystal-field splitting of each J level and the mixture of one with another.

SmNiAl$_4$Ge$_2$ exhibits antiferromagnetic ordering below $T_N = 15.9(1)$ K. The susceptibility was fitted using the Hamaker equation in the temperature region between 25 and 110 K (Fig. 5), resulting in fit parameters of $\mu_{eff} = 0.77(1)$ μ_B, $\theta_p = -30.5(1)$ K and $\delta = 247(2)$ K (red curve, Fig. 4). The effective magnetic moment is slightly smaller than the value of 0.845 μ_B of the free ion, $\delta = 247(2)$ K corresponds to $\Delta E = 706$ K. The energy difference is smaller compared to the value of 1550 K predicted by Stewart, however, a look into the literature reveals that several compounds were shown to exhibit lower values. $\Delta E = 454$ K are found for Sm$_3$Pt$_4$Ge$_6$ [66], 850 K for SmOs$_4$Sb$_{12}$ [67], 1080 K for SmRh$_4$B$_4$ [64], 412, 265, and 1488 K for SmCo$_2$Zn$_{20}$, SmRu$_2$Zn$_{20}$, and SmPd$_2$Cd$_{20}$ [68], 1346 K for SmPdGa$_3$ [69], 1366 K for HP-SmPdSn [70], but also even higher values such as $\Delta E = 2691$ K for SmPt$_6$Al$_3$ are known [71].

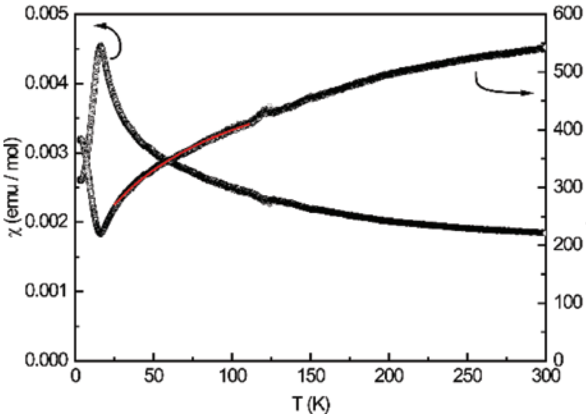

Fig. 5: Temperature dependence of the magnetic susceptibility (χ and χ^{-1} data) of $SmNiAl_4Ge_2$, the fit using the van Vleck law is depicted as red curve [64].

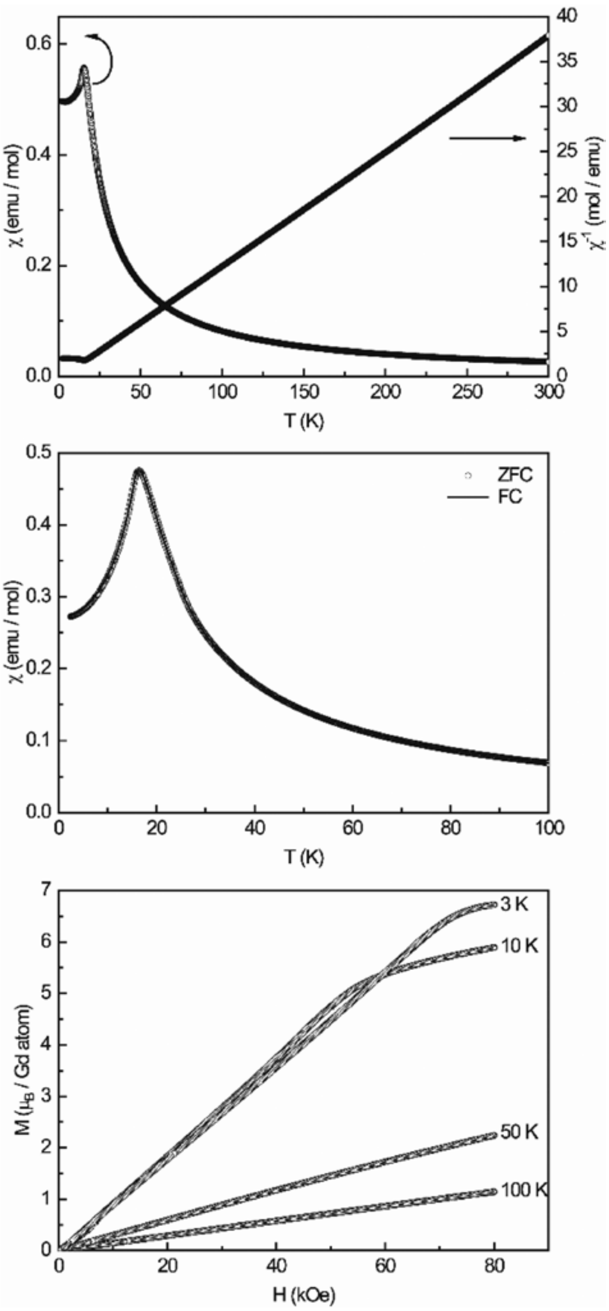

Fig. 6: Magnetic properties of $GdNiAl_4Ge_2$: (top) temperature dependence of the magnetic susceptibility (χ and χ^{-1} data) measured at 10 kOe; (middle) magnetic susceptibility in ZFC/FC mode at 100 Oe; (bottom) magnetization isotherms at $T = 3$, 10, 50 and 100 K.

Fig. 6 depicts the magnetic data of $GdNiAl_4Ge_2$. The top panel shows the χ and χ^{-1} data. The Curie-Weiss fits yielded an effective magnetic moment of $\mu_{eff} = 8.09(1)\ \mu_B$, slightly above the theoretical value of $\mu_{calc} = 7.94\ \mu_B$, pointing towards 4*f*-5*d* hybridization effects. The paramagnetic Curie temperature is $\theta_P = +1.2(1)$ K. The low field measurements (Fig. 6, middle) have confirmed the antiferromagnetic ordering (AFM), already observed in the high-field measurements. The Néel temperature is $T_N = 16.4(1)$ K, and no bifurcation between the ZFC and FC curves is visible. The magnetization isotherms at 50 and 100 K (Fig. 6, bottom) finally exhibit a linear trend, as expected for paramagnetic materials. The 3 and 10 K isotherms, both below the AFM transition, exhibit a slightly curved behavior, indicating a rather stable antiferromagnetic ground state. The ordered spin state gets gradually destroyed with increasing field, leading to a saturation magnetization of $\mu_{sat} = 6.73(1)\ \mu_B$ (3 K, 80 kOe), the expected saturation being 7 μ_B according to $g_J \times J$.

Figure 7 finally depicts the magnetic data of $TbNiAl_4Ge_2$. The Curie-Weiss fit yielded an effective magnetic moment of $\mu_{eff} = 9.76(1)\ \mu_B$ that is in good agreement with the theoretical value of $\mu_{calc} = 9.72\ \mu_B$, and the paramagnetic Curie temperature is $\theta_P = +2.7(1)$ K. The Néel temperature is $T_N = 9.7(1)$ K, and a small bifurcation between the ZFC and FC curve is visible, pointing to traces of ferromagnetic impurities. The magnetization isotherms above the ordered state (50 and 100 K, Fig. 7, bottom) exhibit a linear trend indicating paramagnetic behavior. The 10 K isotherm is curved due to the proximity of the Néel temperature, while for the 3 K isotherm an S-shaped behavior can be observed. This feature is called a meta-magnetic step or spin reorientation, where the antiferromagnetic ground state is turned into a ferromagnetic state upon increasing the field. The ordered antiferromagnetic state gets gradually destroyed, therefore a broad maximum can be observed in the first derivative of the 3 K isotherm leading to a critical field of $H_{crit} = 10(1)$ kOe. The saturation magnetization is $\mu_{sat} = 6.61(1)\ \mu_B$ (3 K, 80 kOe), the expected saturation is 9 μ_B according to $g_J \times J$.

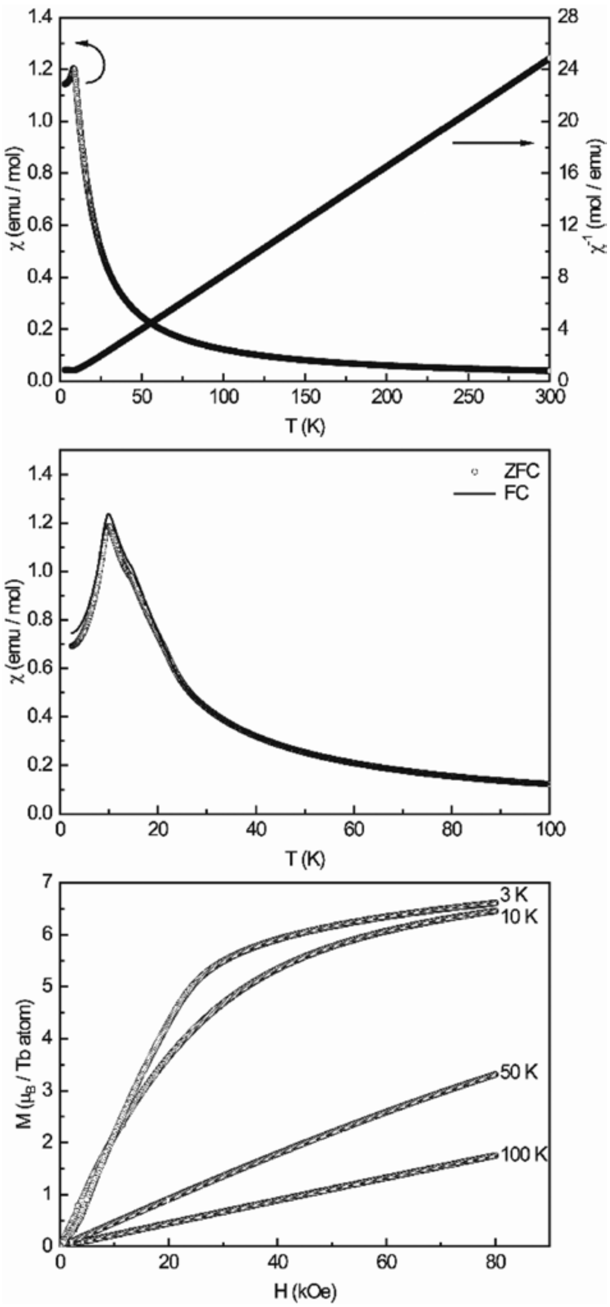

Fig. 7: Magnetic properties of $TbNiAl_4Ge_2$: (top) temperature dependence of the magnetic susceptibility (χ and χ^{-1} data) measured at 10 kOe; (middle) magnetic susceptibility in ZFC/FC mode at 100 Oe; (bottom) magnetization isotherms at $T = 3$, 10, 50 and 100 K.

3.4 ^{27}Al solid-state NMR spectroscopy

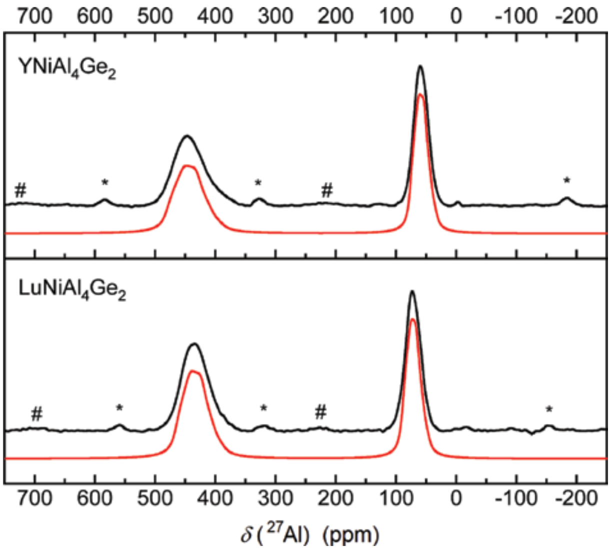

Fig. 8: ^{27}Al MAS-NMR spectra of $YNiAl_4Ge_2$ (top, recorded at a rotor frequency of 40.0 kHz) and $LuNiAl_4Ge_2$ (bottom, recorded at a rotor frequency of 37.0 kHz). Spinning sidebands arising from the non-central transitions of Al1 and Al2 are marked with the symbols * and #, respectively. Tentative line shape simulations based on non-axially symmetric electric field gradients are shown in red.

Figure 8 shows the solid-state ^{27}Al MAS-NMR spectra of the central transition region for $YNiAl_4Ge_2$ and $LuNiAl_4Ge_2$ measured at $B_0 = 14.1$ T. For both compounds, two distinct resonances are observed in an approximate 1:1 ratio, confirming the presence of two crystallographically distinct aluminum sites in the crystal structures. To extract the relevant interaction parameters for these species, one would normally simulate the corresponding line-shapes on the basis of second-order quadrupolar perturbations, using e.g. the program DMFIT [45]. In the present case, such tentative simulations are shown in Fig. 8, but produce unsatisfactory results. They apparently suggest non-axially symmetric electric field gradients characterized by an asymmetry parameter η of close to 0.3, despite the fact that both Al species reside on sites with three-fold rotational symmetry (point group $3m$). Furthermore, for the low-frequency signal the difficulty arises, that the line-shape features are not sufficiently distinct to allow an unambiguous simulation in terms of an axially symmetric field gradient. Rather, it appears that the MAS-NMR line shapes of these aluminum species are additionally influenced by distributions of isotropic magnetic (de-)shielding (and possibly electric field gradients), which might arise from structural (stacking faults) or site occupancy disordering effects. To obtain further insights, triple-quantum (TQ)-MAS-NMR data was measured (Fig. 9). For both compounds, the line-shapes associated with the high-frequency signal can be observed with much better precision than in regular MAS-NMR spectra by analyzing the TQMAS sub-spectra ("slices") obtained at the fixed frequency corresponding to the center of gravity in the F1 dimension. Using this approach (method 1), the nearly axially symmetric electric field gradient for the high-frequency signals near +482

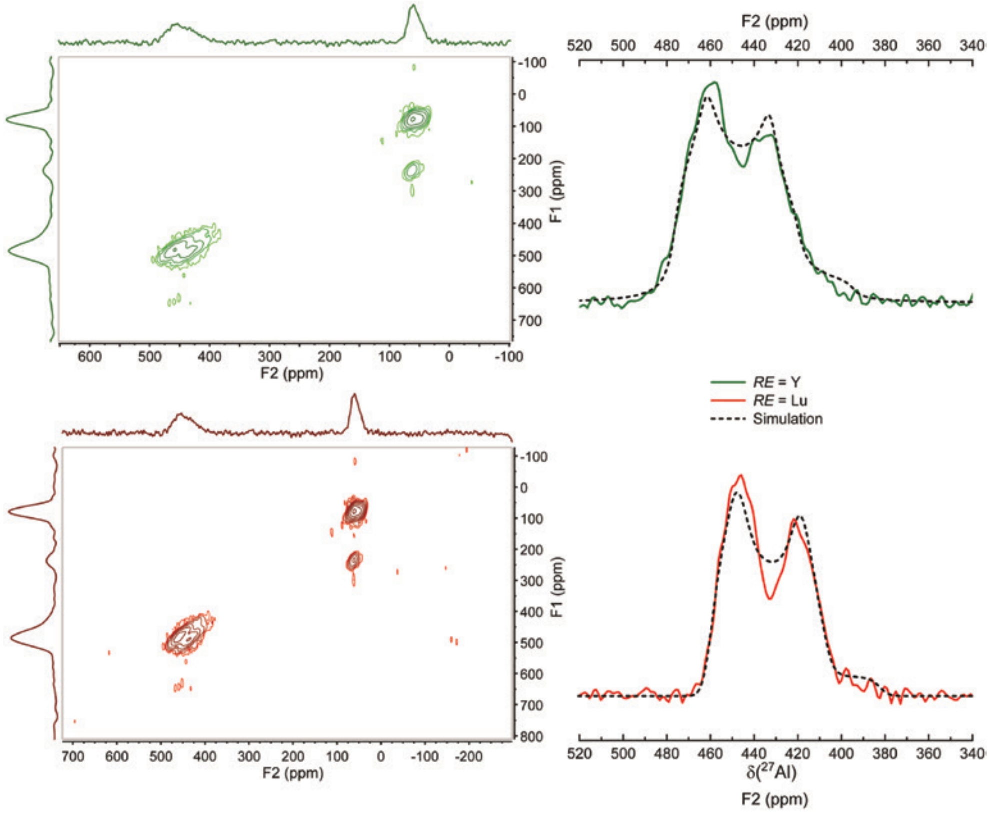

Fig. 9: (left) ^{27}Al TQMAS-NMR spectra of YNiAl$_4$Ge$_2$ and LuNiAl$_4$Ge$_2$. (right) Sub-spectra obtained for the Al1 site obtained at the fixed frequency corresponding to the center of gravity in the F1 dimension, and comparison with the simulated spectrum (dashed curves).

and +467 ppm is clearly revealed in both compounds, whereas this method still turns out to be unsatisfactory for the low-frequency signals. Alternatively the 2D spectra can be analyzed in terms of isotropic magnetic (de-)shielding $\delta_{\text{iso}}^{\text{ms}}$ and the second-order quadrupolar effects ($SOQE = C_Q(1+\eta^2/3)^{1/2}$) by comparing the centers of gravity in the F1 and F2 dimensions [72] (method 2). Table 6 summarizes the line shape parameters obtained for the high-frequency signal by both methods, where the observed discrepancies (~±10 ppm for magnetic (de-)shielding and ~±1 MHz for C_Q) give an impression of the potential systematic errors associated with these different analysis methods. For the low-frequency signal only method 2 produced satisfactory results; thus no independent information regarding the asymmetry parameter is available here.

The assignments of the two signals observed for the two distinct crystallographic sites Al1 and Al2 are based on the comparison of the experimental C_Q or *SOQE* data with predicted values based on electric field gradient calculations, as listed in Table 7. Furthermore, the significant difference in the isotropic magnetic (de-)shielding contributions, $\delta_{\text{iso}}^{\text{ms}}$, between Al1 and Al2 signifies a large difference between the *s*-density of states (*s*-DOS) at the Fermi level for these two aluminum species. While the values measured for Al1 are comparable to those obtained in numerous other intermetallic compounds [18, 20, 22, 75], resulting in a substantial Knight shift contribution,

Table 6: Summary of NMR parameters extracted from the ^{27}Al MAS-NMR spectra for YNiAl$_4$Ge$_2$ and LuNiAl$_4$Ge$_2$; isotropic magnetic deshielding relative to 1 M Al(NO$_3$)$_3$ solution, $\delta_{\text{iso}}^{\text{ms}}$ (±1 ppm), quadrupolar coupling constant C_Q (±1.0 MHz), electric field gradient asymmetry parameter η_Q (±0.05), and *SOQE* parameter (±1.0 MHz) deduced from F1/F2 comparison and fractional area (±3%) of the Al1 and Al2 signals.

	δ_{iso} (ppm)	C_Q (MHz)	η_Q	δ_{iso} (ppm)	*SOQE* (MHz)	Fraction (%)
YNiAl$_4$Ge$_2$						
Al1	482^a	11.9^a	0.30^a	469^b	9.9^b	53^c
Al2				69^b	7.9^b	47^c
LuNiAl$_4$Ge$_2$						
Al1	467^a	11.6^a	0.25^a	458^b	10.1^b	51^c
Al2				85^b	6.3^b	49

^{a}Simulation of the spectra of Figure 9 right (method 1). ^{b}F1/F2 Center of gravity analysis of the TQ spectra (method 2). ^{c}Integration analysis of Figure 8.

Table 7: Calculated quadrupolar coupling constants C_Q, asymmetry parameters η, the quadrupole moments Q as well as the principal components of the electric field gradient tensor (V_{ii} in V/Å^2) for YNiAl$_4$Ge$_2$ and LuNiAl$_4$Ge$_2$.

Atom	C_Q (MHz)	η (V Å^{-2})	Q (mb) [73, 74]	V_{xx} (V Å^{-2})	V_{yy} (V Å^{-2})	V_{zz} (V Å^{-2})
YNiAl$_4$Ge$_2$						
Y	0	–	0	−4.84(1)	−4.84(1)	+9.69(1)
Ni	−1.21(1)	0.0033(3)	+162	+1.54(1)	+1.54(1)	−3.08(1)
Al1	+8.80(1)	0	+146.6	−12.42(1)	−12.42(1)	+24.83(1)
Al2	−6.62(1)	0	+146.6	+9.34(1)	+9.34(1)	−18.68(1)
Ge	+0.31(1)	0.0003(2)	−196	+0.33(1)	+0.33(1)	+0.33(1)
LuNiAl$_4$Ge$_2$						
Lu	+149.02(2)	0	+3490	−8.83(1)	−8.83(1)	+17.66(1)
Ni	−0.48(1)	0.0167(5)	+162	+0.62(1)	+0.62(1)	−1.22(1)
Al1	+9.55(1)	0	+146.6	−13.46(1)	−13.46(1)	+26.93(1)
Al2	−7.01(1)	0	+146.6	+9.90(1)	+9.90(1)	−19.72(1)
Ge	−2.48(1)	0	−196	−2.61(1)	−2.61(1)	+5.23(1)

the δ_{iso}^{ms} value for the Al2 site indicates a much smaller Knight shift. This result is consistent with the band structure calculations revealing also a significant difference between the *s*-DOS of Al1 and Al2 (*vide infra*). Finally, we note that mere reliance on the single-pulse MAS spectra at $B_0 = 14.1$ T would have resulted in the wrong scientific conclusion of non-axially symmetric sites for both Al1 and Al2. Most likely the deviation of the ^{27}Al MAS-NMR line shape from that theoretically expected for axial symmetry is due to the effect of disordering phenomena causing a distribution of isotropic magnetic shielding contributions, which results in a loss of the distinct MAS-NMR line shape features. This distribution effect is also evident in the 2D TQ-MAS-NMR spectrum, which shows a distinct sloping effect in the direction of the diagonal, as a consequence of a distribution of isotropic magnetic (de-)shielding effects. The axial symmetry of the local environments of Al1 and Al2 is further confirmed by additional spectra measured at a lower magnetic field strength ($B_0 = 5.7$ T, data not shown), where the effect of quadrupolar interactions on the MAS-NMR line shapes is significantly stronger, while the influence of isotropic magnetic (de-)shielding distributions is reduced at the lower field strengths. Thus, the results of the present study highlight the importance of MAS and TQ-MAS work for the extraction of reliable NMR parameters if distribution effects of different interaction parameters (such as isotropic magnetic (de-)shielding and quadrupolar coupling) are present.

3.5 Quantum-chemical calculations

The electronic structures of YNiAl$_4$Ge$_2$ and LuNiAl$_4$Ge$_2$ have been calculated and their densities of states (DOS) are presented in Fig. 10. Both compounds are metallic as indicated by the non-zero DOS at the Fermi level (E_F). The *f* states of Lu at –5.5 eV, which are absent for Y, are the only significant difference between the DOS of YNiAl$_4$Ge$_2$ and LuNiAl$_4$Ge$_2$.

At low energies around –10 eV the DOS consists mainly of Ge states, while the 3*d* orbitals of Ni dominate between −4 and –1 eV. Around E_F, between –1 and +1 eV, a deep pseudo-gap is observed indicating electronic stability. Above +1 eV, unoccupied states of Y or Lu in the respective compounds are contributing most to the total DOS. At E_F all the elements contribute almost equally to the total DOS. However, the partial DOS with *s* character for an Al1 atom in YNiAl$_4$Ge$_2$ is 0.0147 states per eV for the individual atom at E_F and thus almost twice as large as for an Al2 atom, for which the partial DOS with *s* character is only 0.0083 states per eV at E_F. Likewise for LuNiAl$_4$Ge$_2$ the *s*-DOS is 0.0156 states per eV for an Al1 atom at E_F and therefore higher as for an Al2 atom, for which the partial DOS with *s* character is only 0.0123 states per eV at E_F. These differences in the *s*-DOS at E_F reflects the difference of the isotropic magnetic de-shielding contributions, δ_{iso}^{ms}, observed in the solid-state ^{27}Al MAS-NMR measurements.

The calculated NMR parameters for YNiAl$_4$Ge$_2$ and LuNiAl$_4$Ge$_2$ are provided in Table 7. Comparing the corresponding results of the calculations with the experimental quadrupolar coupling constants C_Q, the NMR signal at +482 ppm can be assigned to Al1. The signal at +69 ppm with the much weaker quadrupole interaction on the other hand most likely corresponds to Al2. Similarly, the two ^{27}Al solid-state NMR signals in the spectra of LuNiAl$_4$Ge$_2$ can be assigned to Al1 (+467 ppm) and Al2 (+85 ppm).

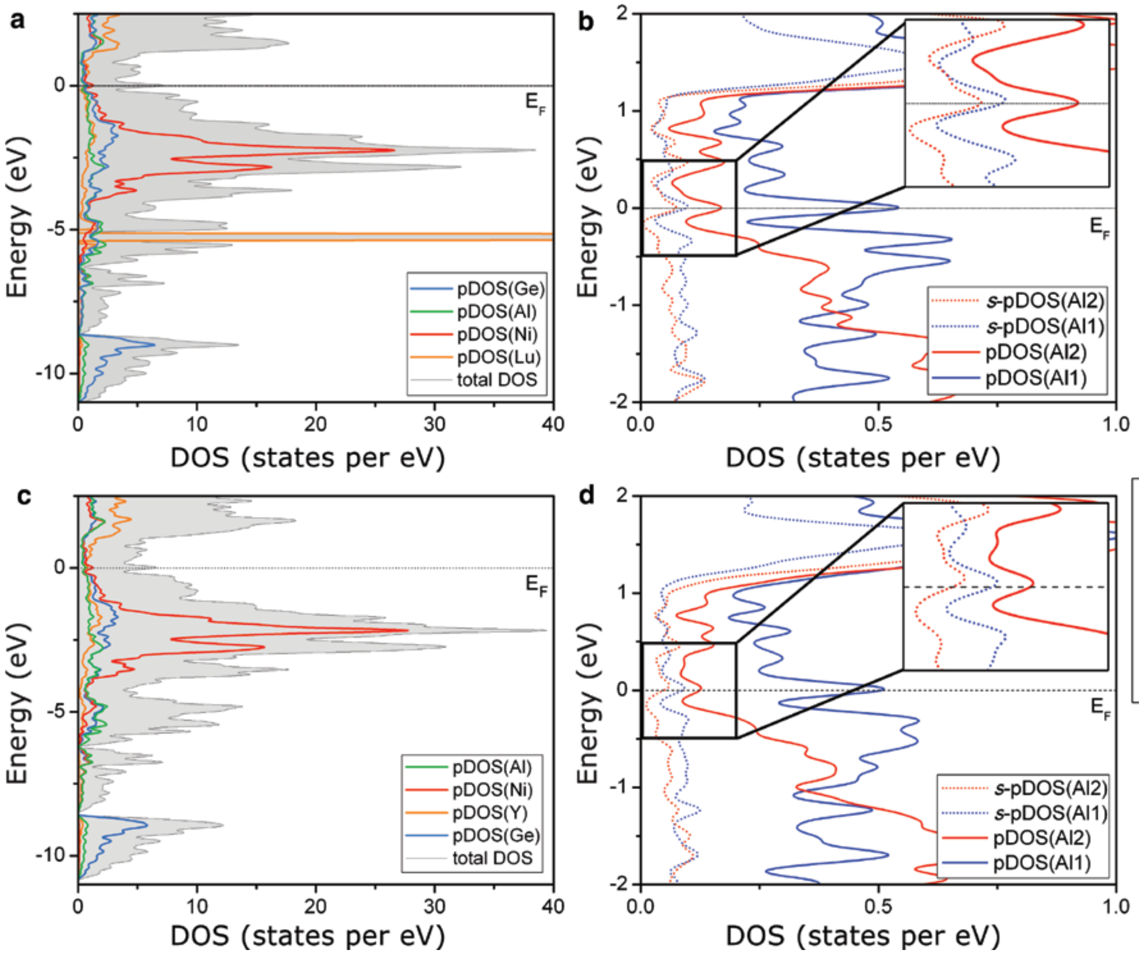

Fig. 10: DOS of $LuNiAl_4Ge_2$ (a) and $YNiAl_4Ge_2$ (c) with the partial DOS indicated by colored lines. The Fermi level E_F (dashed line) is set to 0 eV. The pDOS corresponding to the two Al sites are shown in b and d, respectively.

Finally, the Bader charge analysis reveals almost equal charges on Al1, Al2 and Y of ca. +1.5 for all of them (Table 8). These charges are significantly smaller than +3 for both Al and Y, which indicates that these elements are involved in significant covalent bonding interactions. According to these calculations, the Ge atoms are the respective anions with a charge of −2.15, while the Ni atoms exhibit a calculated charge of −3.15. While the relative charge distributions among cations and anions are in accord with the electronegativities of the elements, the large difference in absolute values between the anions is somewhat surprising as Ni has only a slightly smaller electronegativity than Ge [76]. The Bader charges of $LuNiAl_4Ge_2$ are comparable to those of $YNiAl_4Ge_2$.

Table 8: Calculated Bader charges for $YNiAl_4Ge_2$ and $LuNiAl_4Ge_2$.

Atom	Bader charge	Atom	Bader charge
Y	+1.56(1)	Lu	+1.52(1)
Ni	−3.15(1)	Ni	−3.35(1)
Al1	+1.44(1)	Al1	+1.49(1)
Al2	+1.50(1)	Al2	+1.47(1)
Ge	−2.15(1)	Ge	−2.13(1)

4 Conclusions

The series of the quaternary rare earth nickel aluminum germanides $RENiAl_4Ge_2$ crystallizing in the $SmNiAl_4Ge_2$-type structures has been extended to the rare earth elements *RE* = Y, Sm, Gd–Tm, Lu. All compounds have been investigated by powder X-ray diffraction experiments. Their lattice parameters exhibit the expected decrease due to the lanthanide contraction. The crystal structures of $YNiAl_4Ge_2$, $GdNiAl_4Ge_2$ and $LuNiAl_4Ge_2$ have additionally been studied by single-crystal X-ray diffraction, for which the crystals have been grown in an aluminum flux. The crystal structure can be described as a stacking of two kinds of slabs along the *c* axis, with hexagonal $RE^{\delta+}$ layers alternating with anionic $[NiAl_4Ge_2]^{\delta-}$ slabs. This stacking, however, can cause disorder manifested in stacking faults giving rise to problems in the interpretation of the NMR spectroscopic data. A Bader charge analysis performed on $YNiAl_4Ge_2$ and $LuNiAl_4Ge_2$ has revealed high negative charges on Ge and Ni, which agree well with the initial structure description of anionic slabs. Despite the high charges, the compounds exhibit significant covalent bonding and metallic character. ^{27}Al MAS-NMR spectra can differentiate between the two crystallographic Al sites as is also suggested by quantum chemical electric field gradient calculations, which allow unambiguous peak assignments. The isotropic magnetic de-shielding values confirm the large difference in the *s*-DOS at the Fermi level for the two sites. The Y- and Lu-based compounds are diamagnetic, whereas the Sm-, Gd- and Tb-based analogues show antiferromagnetic ordering below 20 K.

Acknowledgments: We thank Dr. Rolf-Dieter Hoffmann and Dipl.-Ing. Jutta Kösters for the collection of the single crystal intensity data. C.D. acknowledges support by FAPESP grant 2017/06649-0 for a postdoctoral fellowship.

References

[1] R. Ferro, A. Saccone, *Intermetallic Chemistry*, Pergamon, Oxford, Amsterdam, **2008**.
[2] J. Dshemuchadse, W. Steurer, *Intermetallics*, International Union of Crystallography, Oxford University Press, Oxford, **2016**.
[3] R. Pöttgen, D. Johrendt, *Intermetallics – Synthesis, Structure, Function*, 2nd ed., De Gruyter, Berlin, Boston, **2019**.
[4] F. Laves, H. Witte, *Metallwirtschaft* **1935**, *14*, 645.
[5] E. A. Owen, Y. H. Liu, *Philos. Mag.* **1947**, *38*, 354.
[6] H. N. Nowotny, *Z. Metallkd.* **1942**, *34*, 247.
[7] W. L. Bragg, *Proc. R. Soc. London A* **1914**, *89*, 468.
[8] W. P. Davey, F. G. Wick, *Phys. Rev.* **1921**, *17*, 403.
[9] P. Villars, K. Cenzual, *Pearson's Crystal Data: Crystal Structure Database for Inorganic Compounds (on DVD)*, ASM International®, Materials Park, Ohio (USA) **release 2018/2019**.
[10] Z. Ban, M. Sikirica, *Acta Crystallogr.* **1965**, *18*, 594.
[11] B. Eisenmann, N. May, W. Müller, H. Schäfer, *Z. Naturforsch.* **1972**, *27b*, 1155.
[12] C. B. Shoemaker, D. P. Shoemaker, *Acta Crystallogr.* **1965**, *18*, 900.
[13] R. Ferro, R. Marazza, G. Rambaldi, *Z. Metallkd.* **1974**, *65*, 37.
[14] O. Janka, O. Niehaus, R. Pöttgen, B. Chevalier, *Z. Naturforsch.* **2016**, *71b*, 737.
[15] R. Pöttgen, O. Janka, B. Chevalier, *Z. Naturforsch.* **2016**, *71b*, 165.
[16] R. Pöttgen, B. Chevalier, *Z. Naturforsch.* **2015**, *70b*, 289.
[17] R. Pöttgen, B. Chevalier, *Z. Naturforsch.* **2015**, *70b*, 695.
[18] C. Benndorf, H. Eckert, O. Janka, *Acc. Chem. Res.* **2017**, *50*, 1459.
[19] F. Stegemann, C. Benndorf, Y. Zhang, M. Bartsch, H. Zacharias, B. P. T. Fokwa, H. Eckert, O. Janka, *Inorg. Chem.* **2017**, *56*, 1919.
[20] F. Stegemann, C. Benndorf, Y. Zhang, M. Bartsch, H. Zacharias, B. P. T. Fokwa, H. Eckert, O. Janka, *Z. Anorg. Allg. Chem.* **2017**, *643*, 1379.
[21] C. Benndorf, F. Stegemann, S. Seidel, L. Schubert, M. Bartsch, H. Zacharias, B. Mausolf, F. Haarmann, H. Eckert, R. Pöttgen, O. Janka, *Chem. Eur. J.* **2017**, *23*, 4187.
[22] F. Stegemann, T. Block, S. Klenner, Y. Zhang, B. P. T. Fokwa, A. Timmer, H. Mönig, C. Doerenkamp, H. Eckert, O. Janka, *Chem. Eur. J.* **2019**, *25*, 10735.
[23] C. Benndorf, F. Stegemann, H. Eckert, O. Janka, *Z. Naturforsch.* **2015**, *70b*, 101.
[24] F. Eustermann, F. Stegemann, S. Gausebeck, O. Janka, *Z. Naturforsch.* **2018**, *73b*, 819.
[25] M. Radzieowski, F. Stegemann, T. Block, J. Stahl, D. Johrendt, O. Janka, *J. Am. Chem. Soc.* **2018**, *140*, 8950.
[26] F. Stegemann, T. Block, S. Klenner, O. Janka, *Chem. Eur. J.* **2019**, *25*, 3505.
[27] F. Stegemann, J. Stahl, M. Bartsch, H. Zacharias, D. Johrendt, O. Janka, *Chem. Sci.* **2019**, *10*, 11086.
[28] N. J. Ghimire, S. K. Cary, S. Eley, N. A. Wakeham, P. F. S. Rosa, T. Albrecht-Schmitt, Y. Lee, M. Janoschek, C. M. Brown, L. Civale, J. D. Thompson, F. Ronning, E. D. Bauer, *Phys. Rev. B* **2016**, *93*, 205141.
[29] P. Demchenko, J. Kończyk, G. Demchenko, R. Gladyshevskii, V. Pavlyuk, *Acta Crystallogr.* **2006**, *C62*, i29.
[30] B. Sieve, P. N. Trikalitis, M. G. Kanatzidis, *Z. Anorg. Allg. Chem.* **2002**, *628*, 1568.
[31] G. Demchenko, J. Kończyk, P. Demchenko, R. E. Gladyshevskii, W. Majzner, L. Muratova, *Chem. Met. Alloys* **2008**, *1*, 254.
[32] G. Demchenko, P. Y. Demchenko, *Visn. Lviv. Derzh. Univ., Ser. Khim.* **2010**, *51*, 45.
[33] N. Z. Semuso, Y. Y. Lutsyshyn, S. Y. Pukas, Y. A. Tokaychuk, R. E. Gladyshevskii, *Ukr. Khim. Zh.* **2015**, *81*, 36.
[34] J. T. Zhao, E. Parthe, *Acta Crystallogr.* **1990**, *C46*, 2273.
[35] G. Demchenko, J. Kończyk, P. Demchenko, O. Bodak, B. Marciniak, *Acta Crystallogr.* **2005**, *E61*, i273.
[36] C. Zeng, G. Lin, W. Zeng, W. He, *Powder Diffr.* **2015**, *30*, 63.
[37] G. Demchenko, P. Y. Demchenko, R. E. Gladyshevskii, *Visn. Lviv. Derzh. Univ., Ser. Khim.* **2008**, *49*, 103.
[38] W. He, W. Zeng, G. Lin, *J. Alloys Compd.* **2015**, *627*, 307.
[39] N. Z. Semuso, Y. Lutsyshyn, S. Y. Pukas, Y. Tokaychuk, R. E. Gladyshevskii, *Visn. Lviv. Derzh. Univ., Ser. Khim.* **2016**, *57*, 89.
[40] X. Wu, M. G. Kanatzidis, *J. Solid State Chem.* **2005**, *178*, 3233.
[41] B. Sieve, X. Chen, J. Cowen, P. Larson, S. D. Mahanti, M. G. Kanatzidis, *Chem. Mater.* **1999**, *11*, 2451.
[42] R. Pöttgen, T. Gulden, A. Simon, *GIT Labor-Fachz.* **1999**, *43*, 133.
[43] P. J. Becker, P. Coppens, *Acta Crystallogr.* **1974**, *A30*, 129.
[44] J. C. C. Chan, H. Eckert, *J. Non-Cryst. Solids* **2001**, *284*, 16.
[45] D. Massiot, F. Fayon, M. Capron, I. King, S. Le Calvé, B. Alonso, J.-O. Durand, B. Bujoli, Z. Gan, G. Hoatson, *Magn. Reson. Chem.* **2002**, *40*, 70.
[46] P. E. Blöchl, *Phys. Rev. B* **1994**, *50*, 17953.
[47] G. Kresse, D. Joubert, *Phys. Rev. B* **1999**, *59*, 1758.
[48] G. Kresse, J. Furthmüller, *Phys. Rev. B* **1996**, *54*, 11169.
[49] G. Kresse, J. Furthmüller, *Comput. Mater. Sci.* **1996**, *6*, 15.
[50] J. P. Perdew, K. Burke, M. Ernzerhof, *Phys. Rev. Lett.* **1996**, *77*, 3865.
[51] H. J. Monkhorst, J. D. Pack, *Phys. Rev. B* **1976**, *13*, 5188.
[52] E. Sanville, S. D. Kenny, R. Smith, G. Henkelman, *J. Comput. Chem.* **2007**, *28*, 899.
[53] G. Henkelman, A. Arnaldsson, H. Jónsson, *Comput. Mater. Sci.* **2006**, *36*, 354.

[54] W. Tang, E. Sanville, G. Henkelman, *J. Phys.: Condens. Matter* **2009**, *21*, 084204.
[55] L. Palatinus, G. Chapuis, *J. Appl. Crystallogr.* **2007**, *40*, 786.
[56] V. Petříček, M. Dušek, L. Palatinus, JANA2006, The Crystallographic Computing System, Institute of Physics, Academy of Sciences of the Czech Republic, Prague (Czech Republic) **2006**.
[57] V. Petříček, M. Dušek, L. Palatinus, *Z. Kristallogr.* **2014**, *229*, 345.
[58] R. D. Shannon, C. T. Prewitt, *Acta Crystallogr.* **1969**, *B25*, 925.
[59] R. D. Shannon, *Acta Crystallogr.* **1976**, *A32*, 751.
[60] J. Vannimenus, G. Toulouse, *J. Phys.: Solid State Phys.* **1977**, *10*, L537.
[61] G. Toulouse, in *Modern Trends in the Theory of Condensed Matter* (Eds.: A. Pękalski, J. A. Przystawa), Springer Berlin Heidelberg, Berlin, Heidelberg, **1980**, p. 195.
[62] E. O. Wollan, W. C. Koehler, *Phys. Rev.* **1955**, *100*, 545.
[63] A. M. Stewart, *Phys. Rev. B* **1972**, *6*, 1985.
[64] H. C. Hamaker, L. D. Woolf, H. B. MacKay, Z. Fisk, M. B. Maple, *Solid State Commun.* **1979**, *32*, 289.
[65] A. M. Stewart, *Phys. Rev. B* **1993**, *47*, 11242.
[66] F. Eustermann, M. Eilers-Rethwisch, K. Renner, R.-D. Hoffmann, R. Pöttgen, O. Janka, *Z. Naturforsch.* **2017**, *72b*, 855.
[67] W. M. Yuhasz, N. A. Frederick, P. C. Ho, N. P. Butch, B. J. Taylor, T. A. Sayles, M. B. Maple, J. B. Betts, A. H. Lacerda, P. Rogl, G. Giester, *Phys. Rev. B* **2005**, *71*, 104402.
[68] D. Yazici, B. D. White, P. C. Ho, N. Kanchanavatee, K. Huang, A. J. Friedman, A. S. Wong, V. W. Burnett, N. R. Dilley, M. B. Maple, *Phys. Rev. B* **2014**, *90*, 144406.
[69] S. Seidel, O. Niehaus, S. F. Matar, O. Janka, B. Gerke, U. C. Rodewald, R. Pöttgen, *Z. Naturforsch.* **2014**, *69b*, 1105.
[70] G. Heymann, B. Heying, U. C. Rodewald, O. Janka, H. Huppertz, R. Pöttgen, *J. Solid State Chem.* **2016**, *236*, 138.
[71] F. Eustermann, F. Stegemann, K. Renner, O. Janka, *Z. Anorg. Allg. Chem.* **2017**, *643*, 1836.
[72] A. Medek, L. Frydman, *J. Braz. Chem. Soc.* **1999**, *10*, 263.
[73] P. Pyykkö, *Mol. Phys.* **2001**, *99*, 1617.
[74] P. Pyykkö, *Mol. Phys.* **2008**, *106*, 1965.
[75] M. Radzieowski, F. Stegemann, C. Doerenkamp, S. F. Matar, H. Eckert, C. Dosche, G. Wittstock, O. Janka, *Inorg. Chem.* **2019**, *58*, 7010.
[76] A. L. Allred, E. G. Rochow, *J. Inorg. Nucl. Chem.* **1958**, *5*, 264.